The evolving energy budget of experimental faults within continental crust: Insights from *in situ* dynamic X-ray microtomography

Jessica McBeck[1], Benoit Cordonnier [1], Karen Mair[1], François Renard[1,2]

1 Physics of Geological Processes, The Njord Centre, Department of Geosciences, University of Oslo, Norway
2 University Grenoble Alpes, University Savoie Mont Blanc, CNRS, IRD, IFSTTAR, ISTerre, Grenoble, France

Highlights

- Calculation of energy budget throughout experiments with sliding precut fault.
- Frictional work consumes 50-100% of the energy budget.
- Internal work consumes 5-20% of the energy budget.
- Greater fault roughness increases the episodicity of slip.
- Greater fault roughness increases the width and asymmetry of the damage zone.

Corresponding author
Jessica McBeck
j.a.mcbeck@geo.uio.no
https://orcid.org/0000-0002-4465-5522

Keywords
fault; friction; damage zone; energy budget; digital volume correlation; X-ray microtomography

Abstract

We investigate the evolving distribution of strain produced by a sliding fault within intact crystalline rock, and the energetics of deformation that occur both on- and off-fault. We slid precut faults of differing roughness oriented at 45° to σ_1 while acquiring *in situ* X-ray microtomograms. Digital volume correlation of these time series of 3D local density fields provide estimates of the 3D displacement and strain fields. Our novel representation and sampling of the strain tensor field reveal that the differing fault roughness produced distinct slip behavior, degree of strain localization and accumulation, and energy budget partitioning. The rougher fault slipped more episodically, hosted a wider and more asymmetric damage zone, and accommodated less normal and shear strain. This fault consumed more energy in off-fault deformation (W_{int}) per volume and more energy in frictional slip (W_{fric}) as portions of the total energy input to the system (W_{ext}) than the smoother fault. In both experiments, W_{fric} consumed the largest portion of the energy budget (50-100%), while W_{int} consumed smaller percentages (5-20%). Tracking the temporal variability of energy partitioning revealed how evolving fault architecture determined the energetic dominance of various deformational processes, and so highlighted the importance of tracking energy partitioning through time.

1. Introduction

Constraining the spatial extent and magnitude of off-fault deformation surrounding seismic fault networks can help shed light on the physics that govern earthquake rupture, propagation and cessation, and is critical for accurate measurement of long-term slip rates, and corresponding seismic hazard assessment (e.g., *Wilson et al*., 2005; *Shelef & Oskin*, 2010; *Milliner et al*., 2015). In particular, asymmetric damage zones surrounding seismic faults have been linked to the directionality of earthquake rupture, differences in mechanical properties across faults and the geometric complexity of faults (e.g., *Ben-Zion & Shi*, 2005; *Shi & Ben-Zion*, 2006; *Griffith et al*., 2010). Volumes of subsurface crust with lower shear rigidity surrounding major strike-slip faults provide evidence of damage zones surrounding faults at depth (e.g., *Ben-Zion & Sammis*, 2003). Varying fracture density within damage zones surrounding faults likely influences strain partitioning and localization. However, field techniques struggle to capture the variations in off-fault strain at differing fault-perpendicular distances that arise from damage zones, and cannot provide direct subsurface measurements of strain. Consequently, the degree to which damage zones influence strain localization and partitioning surrounding continental faults remains largely unconstrained.

The amount of energy consumed in elastic off-fault deformation, the internal work, is a concise quantification of the magnitude of stress and strain that damage zones endure. This component of the energy budget differs from the fracture energy, or work to create new fracture surfaces, W_{prop}, within a damage zone (*Cooke and Madden*, 2014). Internal work, W_{int}, may be calculated as the volume integral of the strain energy density of a system (e.g., *Timoshenko & Goodier*, 1951). By assuming that faults will propagate toward regions with high stresses and/or strains, previous workers have used strain energy density to predict fault development (*Cooke and Madden*, 2014 and references therein). *Du & Aydin* (2003) found that the predictions of maximum distortional strain energy density for shear fracture propagation under mixed-mode conditions matched field observations. *Okubo & Shultz* (2005) successfully predicted the nucleation and propagation of compaction bands using the volumetric and distortional components of strain energy density. Varying damage zone volumes and fracture densities within them (e.g., *Faulkner et al*., 2011) provide qualitative means of comparing the W_{int} done in various crustal settings. However, few numerical (e.g., *Del Castello & Cooke*, 2007; *Savage & Cooke*, 2010; *Cooke & Madden*, 2014; *Newman & Griffith*, 2014; *Madden et al*., 2017) or experimental (*McBeck et al*., 2018a) studies have attempted to constrain W_{int} because it is the volume integral of strain energy density, requiring estimates of the full stress and strain tensors. Consequently, the proportion of the energy budget consumed in off-fault deformation within continental crust remains a poorly constrained magnitude.

Another critical component of the complete energy budget is the work done against frictional slip, W_{fric} (e.g., *Cooke and Madden*, 2014). Recent advances in field techniques, such as detecting heat anomalies near seismic faults (*Fulton et al*., 2013) and the thermal maturity of organic material (*Savage et al*., 2014) have provided constraints on the energy expended against frictional slip in crustal environments. Differing estimates of the dynamic friction, μ_d, along accretionary prism megathrusts ($\mu_d = 0.08$; *Fulton et al*., 2013), thrust faults within the Nankai prism ($\mu_d < 0.5$; *Ikari et al*., 2009), actively creeping strands of the San Andreas Fault in the Central Deforming Zone ($\mu_d = 0.1$) and the Northeast Boundary Fault (suggested to host small repeating earthquakes, $\mu_d > 0.4$) (*Carpenter et al*., 2015), and laboratory faults in foliated rocks ($0.2 < \mu_d < 0.4$ for intact rocks; *Collettini et al*., 2009) suggest that the portion of the total energy input consumed by W_{fric} may differ amongst faults in each of these environments. Accordingly, the energy consumed by W_{int} will vary with differences in W_{fric} because the total energy consumed in a system arises from the sum of W_{fric}

and W_{int}. Assuming equal inputs of external work applied to the system, as more work is done in frictional slip, less work may be expended as off-fault deformation.

The energy budget framework provides a concise quantitative method of comparing the contributions of these deformational processes on the total energetics of the system, and differences in these contributions across disparate tectonic environments (Figure 1). Several analyses have used both W_{fric} and the work done in uplift against gravity, W_{grav}, to successfully assess fault development (e.g., *Gutscher et al*., 1998; *Burbidge & Braun*, 2002; *Yagupsky et al*., 2014). The exclusion of W_{int} from these analyses suggests that the contribution of internal work to the overall energy budget was not necessary to consider in order to adequately match the predictions to natural crustal systems. Similarly, calculations of components of the work budget in physical accretionary wedge experiments suggest that the portion of the energy budget consumed in W_{int} is smaller than 1% of the total energy input to the system (*McBeck et al*., 2018a). However, the analytical analysis of *Mitra & Boyer* (1986) found that W_{int}, W_{fric} and W_{grav} are within two orders of magnitude of each other during the formation of duplex fault zones, suggesting that internal work may not be negligible in these tectonic systems, and so important to consider in energy budget analyses. Similarly, *Savage & Cooke* (2010) found that W_{int} exceeds the sum of the other components of the energy budget in linear elastic models of shear faulting that include off-fault tensile fracturing. Furthermore, estimates of W_{int} in linear elastic mechanical models of contracting accretionary wedges range from 25% to 50% throughout an underthrusting-accretion cycle (*Del Castello & Cooke,* 2007).

To investigate the evolution of the energy budget of sliding faults embedded in crystalline rock, and compare the evolving energetic importance of frictional slip and off-fault deformation, we slid precut faults in monzonite rock core samples within the HADES triaxial deformation apparatus (*Renard et al*., 2016) while acquiring X-ray adsorption three-dimensional images, i.e., tomograms. Previous experiments using the HADES apparatus have investigated fault nucleation, strain localization and fracture coalescence in nominally intact rock cores (e.g., *Renard et al.*, 2017; *McBeck et al*., 2018b; *Renard et al*., 2018a, 2018b). Here, we precut the faults rather than deforming intact cores in order to investigate strain localization and energy budget partitioning surrounding localized fault planes. Moreover, the predefined location of the macroscopic fault surface enabled the energy budget analysis and quantification of strain partitioning between the localized slip surface and the off-fault volume. Whereas triaxial deformation experiments on intact cores reveal the progressive localization of fractures into through-going faults that produce macroscopic failure, the experimental system analyzed in this contribution is analogous to geologic systems in which series of earthquakes or aseismic slip events reactivate a discontinuity surrounded by relatively intact rock. The surrounding intact rock may have been damaged in previous earthquakes, but then the microfractures within this volume subsequently healed (e.g., *Tenthorey et al.*, 2003).

The tomograms reveal 3D variations of X-ray adsorption that correspond to variations in local density, and so can pinpoint the geometry of opening fractures. Digital volume correlation (DVC) analysis of pairs of tomograms captured throughout the experiments provides 3D displacement and strain fields. Using the spatial distribution of the normal and shear strains calculated through DVC, we tracked the growth and asymmetry of the damage zones surrounding the faults. Then, we quantified the evolving partitioning of the energy budget as the faults slipped, damage zones thickened, and the surrounding host rock deformed. These experimental observations provide key constraints on critical questions, including: 1) the rate at which damage zones thicken in continental crust, 2) the ability of asymmetric damage zones to develop within the same material, 3) the relative energetic importance of deformational processes in continental tectonic environments with slipping faults, and 4) the evolution of energy budget partitioning with evolving fault architecture.

2. Methods

2.1. Experiment design

We used the X-ray transparent HADES triaxial deformation apparatus (*Renard et al*., 2016) to slide two precut monzonite cores and acquire dynamic X-ray tomograms during deformation. This apparatus, installed on the microtomography beamline ID19 at the European Synchrotron and Radiation Facility, enables *in situ* imaging of rock deformation as rocks are triaxially compressed. Monzonite is an ideal material for deformation in the HADES apparatus and DVC analysis because it contains crystals of plagioclase and feldspar that appear distinct in the X-ray tomograms. The distinct crystals and patterns within monzonite enable calculating displacement fields with digital volume correlation (DVC). Moreover, monzonite is a crystalline rock with frictional and elastic properties similar to many continental crustal rocks, such as granite. Consequently, energy budget partitioning derived from these experiments on monzonite represent that partitioning in continental crustal material. *Renard et al.* (2018b) analyzed the deformation of intact cores of this material, and *Aben et al.* (2016) describe this monzonite in detail, as containing 18% quartz, 13% biotite, 58% plagioclase, 12% clinopyroxene and minor minerals, with 450 μm mean grain size.

To produce the preexisting faults, we cut 10 mm tall, and 5 mm wide cylinders at 45° from the flat surfaces of the cores. We set the orientation of the faults in both experiments to 45° from the direction of σ_1 and the vertically-applied axial displacement. We chose this fault orientation because experiments with gouge-filled precut faults at varying orientations found that 45° marks a transition in deformation behavior in which the fractures propagate into the surrounding host rock, or deformation remains dominantly localized on the precut fault

(*Giorgetti et al*., 2019). Furthermore, the 2:1 aspect ratio of the cores prevented cutting faults oriented 60° from the direction of σ_1, as the tips of the fault intersect the top or bottom of the core, preventing sliding along the fault.

We created the smoother (experiment M6) fault surfaces by sanding the interfaces with grit P2000 sandpapers. We created the rougher fault surfaces by sanding the interfaces with 10 passes of P400 sandpaper, and 3 passes of P80 sandpaper. We measured the root-mean-squared roughness of the slip surface before and after slip of the smoother fault (M6) using a white light interferometer (e.g. *Candela et al*., 2014; *Toy et al*., 2017). The mean of the roughness measured on several squares of 1x1 mm^2 of the unslipped, initial fault surface was 56 µm, and decreased after slip to 6 µm for the smoother fault. We could not measure the roughness of the rougher fault (M8) after the experiment because the blocks of the core failed during the experiment. The mean of the roughness measured on the unslipped fault surface was 228 µm for the rougher fault.

We slid the blocks using approximately constant increments of applied axial shortening, u_z, of 50 µm, as measured from the Linear Variable Differential Transformer (LVDT) displacement sensor of the experimental apparatus. Between each axial displacement step, we acquired *in situ* X-ray tomograms in time intervals of 5-10 minutes and at spatial resolutions of 6.5 µm (Figure 2). The axial displacement step size of 50 µm provides an ideal compromise between a step size large enough to include several voxels of axial displacement in each step and small enough so that each experiment includes several tens of steps. The length of the side of each voxel was 6.5 µm in these experiments. At the conditions of the experiments, with no pore fluid and at ambient temperature, fault healing via growth of asperities and increasing real contact area was unlikely to occur within the scan time of 5-10 minutes. We applied 40 MPa and 50 MPa of confining stress to the smoother and rougher fault experiments, respectively, using silicon oil.

To assess the reproducibility of the experimental results, we conducted a total of four experiments with precut surfaces of varying roughness in monzonite cores within the HADES apparatus. We focus on only two experiments here because the behavior of the other experiments was similar to that observed in these experiments. In particular, these two other experiments had precut surfaces that were prepared with the same technique as the rougher fault experiment. In both experiments, the precut fault initially slid, but then the surrounding host rock failed.

2.2. Digital volume correlation

To examine strain localization surrounding these evolving fault zones, we calculated the incremental 3D internal displacement vectors between successive scans using digital volume correlation (DVC) analysis, implemented in TomoWarp2 (*Tudisco et al*., 2017). The incremental displacements reflect deformation that occurred in the time between tomogram acquisitions. We calculated the internal displacement vectors following the same procedure as previous analyses (*McBeck et al*., 2018b, *Renard et al*., 2018a), including the choice of node spacing size (20 voxels) and correlation window size (10 voxels). The node spacing size and correlation window size control the spatial resolution and detectable displacement strain magnitudes, respectively (e.g., *McBeck et al*., 2018b). However, the large displacements that occur between the acquisitions of the tomogram pairs used in the DVC analysis in these experiments require larger search window sizes than previous calculations. The search window size controls the maximum limit of detected displacements. The combination of these DVC parameters requires 7 hours to calculate the incremental displacements of one tomogram pair using a desktop computer, whereas previous analyses only required 2-3 hours (*McBeck et al*., 2018b, *Renard et al*., 2018a).

Here, we examine both the incremental displacement fields, and incremental strain fields calculated from the displacements. We rotate the coordinates and displacement vectors of the

DVC analysis so that they reflect the fault strike-parallel (*y*-axis) and strike-perpendicular (*x*-axis) positions and displacements. The *z*-axis is vertical and parallel to σ_1 in this coordinate system. Consequently, the resulting strain components of normal horizontal strain, ε_{xx}, normal vertical strain, ε_{zz}, and shear strain, ε_{xz}, arise from a coordinate system based on the fault-strike orientation and direction of σ_1. Dilation is negative and contraction is positive in the adopted sign convention.

To examine the distribution of strain, we built median projections of the 3D strain fields using a 3D slab within the center of the core (Figure S1). The center of this slab volume coincides with the center of the core, and extends 2 mm in thickness parallel to the fault strike (*y*-axis), 2.5 mm in width perpendicular to the fault strike (*x*-axis), and 4.5 mm parallel to σ_1 (*z*-axis). We used this volume in order to avoid artefacts in the calculated displacements near the edges of the core.

2.3. Energy budget analysis

To quantify the energetics of off-fault and on-fault deformation, we calculated the incremental internal work, W_{int}, frictional work, W_{fric} and external work, W_{ext} throughout both experiments. The internal work and frictional work capture the energetics of off- and on-fault deformation, respectively, while the external work captures the total energy input to the system. We calculated these components following the formulations of *Cooke and Madden* (2014), described in detail below. We used the incremental displacements and strains derived from the DVC analysis to calculate the incremental energy budget components. Consequently, these incremental components reflect the work done between the acquisition of each tomogram pair as a result of the imposed axial displacement.

The magnitude of the work budget components depends on the size of the analyzed system. Here, we selected our system as a rectangular prism with the dimensions of the slab used to create the strain median projections, described in Section 2.2 and shown in Figure S1.

We selected this subset of the core in which to calculate the energy budget so that boundary effects, such as unreliable DVC displacements near the core edges, did not bias the calculations. In this volume, we calculated median projections of the incremental displacement and strain fields parallel to the fault surface, producing 2D representations of 3D fields. We used the resulting 2D displacement and strain fields to calculate the energy budget components by integrating these measurements over the 2 mm thick dimension of the volume parallel to the fault plane. This simplification of the system reduces the dependence of the work budget values on local perturbations in the displacement field.

Following the law of conservation of energy, the total external work expended on a system, W_{ext}, must match the sum of the work expended in deformational processes within the system:

$$W_{ext} = W_{int} + W_{grav} + W_{fric} + W_{prop} + W_{seis} \qquad \text{Eq. 1}$$

where W_{int} is the internal work of host rock deformation surrounding faults, W_{grav} is the work against gravity, W_{fric} is the work against friction along faults, W_{prop} is the energy to create fault surfaces, and W_{seis} is the energy of ground shaking (*Cooke and Madden*, 2014). In this contribution, we focus on W_{ext}, W_{int} and W_{fric} because W_{grav} is insignificant at the differential stresses of these triaxial compression experiments, W_{seis} is insignificant at the small and slow slip increments of these experiments, and W_{prop} is the focus of a forthcoming analysis.

Following *Cooke and Madden* (2014), in a two-dimensional system, W_{ext} may be calculated by integrating over the loading path, L, the sum of the products of shear traction and displacement, τ and u_s, and normal traction and displacement, σ_n and u_n, integrated over the system boundaries, B:

$$W_{ext} = \int_L \iint_B (\tau u_s + u_n \sigma_n)\, dB dL \qquad \text{Eq. 2}$$

The incremental external work done between the acquisition of two tomograms, or within any experimental increment, ∂W_{ext}, may be considered to be the area under the force-displacement curve within an increment of deformation, such that

$$\partial W_{ext} = u_n \sigma_n^0 + \frac{1}{2} u_n (\sigma_n^1 - \sigma_n^0) + u_s \tau^0 + \frac{1}{2} u_s (\tau^1 - \tau^0) \qquad \text{Eq. 3}$$

where σ_n^0 and σ_n^1, and τ^0 and τ^1, indicate the normal and shear stresses when the first and second tomograms of the DVC analysis were acquired, and u_n and u_s are the incremental displacements done within this step of the experiment. This formulation follows from the procedure to calculate ∂W_{ext} employed in *McBeck et al*. (2018a).

We constrained the displacements applied to the boundaries of the system from the incremental displacement field calculated from the DVC analysis (Figure S1). We estimated the potential upper and lower ranges of ∂W_{ext} using the mean ± one standard deviation of the displacements observed in 0.1 mm x 0.25 mm rectangles along the system boundaries. The 0.1 mm side of these sampling rectangles were parallel to the face of each boundary and the 0.25 mm side extended within the system perpendicular to this face (Figure S1). We constrained the normal stresses acting on the boundaries of the slab using the principal stresses applied to the tomography scans at their acquisition. The shear stresses along the left and right sides of the system were negligible because of the large difference in stiffness between the rock core and the jacket. The shear stresses along the top and bottom sides of the volume may be non-negligible due to the lack of lubrication along the top and bottom rock-piston interfaces. However, these shear stresses are likely small because the rock and piston interfaces are not fixed to each other and are planar, and so likely have low effective friction coefficients. Consequently, to calculate ∂W_{ext}, we assumed that the shear stresses on the system boundaries are zero.

The incremental frictional work, ∂W_{fric}, depends on the sliding shear stress along the fault, τ, the slip distance, s, and the fault area experiencing slip, A,

$$\partial W_{fric} = |\tau| sA \qquad \text{Eq. 4}$$

We estimated the magnitude of the sliding shear stress using the average of the principal stresses of the two tomograms used in the DVC analysis, σ_1, σ_2, and the prescribed θ=45° orientation of the fault,

$$\tau = \left| \frac{(\sigma_1 - \sigma_2)}{2} \sin 2\left(\frac{\pi}{2} - \theta\right) \right| \qquad \text{Eq. 5}$$

We constrained the incremental fault slip done in one sliding step in the experiment using two methods that provide upper and lower estimates of ∂W_{fric} (Figure S1). In both methods, we extracted the area of the strain fields in which two of the three independent strain components exceed a threshold strain (0.0025). This extracted area represents the fault zone, while the areas outside this zone are considered off-fault. This automated extraction method allows the observed fault zone to vary in width throughout deformation, and in width along the fault. However, we restricted this zone to 0.75 mm outside of the precut surface to ensure that noise in the DVC displacement fields did not contribute to the fault slip estimates. This maximum limit of the fault zone width only influenced the extent of the automatically-extracted fault zone in the final two stages of the rougher fault experiment, as the upper block began to fracture and break. Later, we examine the impact of using different threshold strains to extract the fault zone, and find a minimal impact on the calculated energy components.

The two methods to calculate fault slip that provide upper and lower estimates of ∂W_{fric} use the shear strain field (upper estimate) and displacement vectors (lower estimate) near the fault. We derived the upper estimate of fault slip by integrating the shear strain field within the identified fault zone. We derived the lower estimate using the displacement vectors within this fault zone. In particular, we rotated the displacement vectors by 45° so that the rotated horizontal displacements, $u_{x'}$, represent the fault-plane parallel slip (Figure S2). We found the mean of $u_{x'}$ in regions above and below the fault plane, and added the magnitudes of these vectors to find the total slip. The mean slip vectors in the upper and lower blocks have opposite signs as the upper block moves rightward and the lower block moves slightly leftward or remains relatively stable (Figure S2), so the $|u_{x'}|$ on either side of the fault sum to the total slip.

Using the rotation method of constraining slip likely underestimates the true fault slip because the displacement vectors near the fault tend to decrease in magnitude toward the fault core as correlation of pixel patterns becomes increasingly difficult. Consequently, the mean of $u_{x'}$ may underrepresent the true fault plane-parallel displacement. Integrating the shear strain field in the identified fault zone may tend to overestimate fault slip because it may consider high strains that arise outside of the true fault core as part of the on-fault deformation. Consequently, comparing frictional work estimates derived from these two methods provides constraints on the potential range of frictional work values.

The incremental internal work, ∂W_{int}, depends on components of the stress, σ_{ij}, and strain, ε_{ij}, tensor outside of the fault zone, in a 2D Cartesian coordinate system in the *x*-*z* plane,

$$\partial W_{int} = \frac{1}{2}\iint(\varepsilon_{xx}\sigma_{xx} + \varepsilon_{zz}\sigma_{zz} + 2\varepsilon_{xz}\sigma_{xz})dxdz \qquad \text{Eq. 6}$$

To calculate ∂W_{int}, we sampled the strain fields outside of the identified fault zone (in which ∂W_{fric} is calculated) (Figure S1D). We estimated the stress components from the strain components using Hooke's law. To derive the stresses from the strains with these relationships, we used a range of elastic moduli constrained from our previous experiments on intact cores of monzonite with the HADES deformation apparatus (*Renard et al*., 2018b). This decreasing range of elastic moduli reflects the impact of microfracture development on the host rock stiffness, as higher densities of microcracks tend to reduce rock stiffness (e.g., *Katz & Reches*, 2004). The axial strain-stress relationships of intact monzonite experiments indicate that the effective elastic modulus, *E'*, decreased from 30 GPa to 10 GPa, and 20 GPa to 10 GPa from the onset of loading to immediately preceding macroscopic failure (*Renard et* *al*., 2018b). Consequently, we allow E' to decrease linearly from 30 GPa to 10 GPa (upper estimate) and from 20 GPa to 10 GPa (lower estimate) from the first to the last scan acquired in each experiment. The linear ramps of E' starting at 30 GPa and 20 GPa determines the upper and lower estimates of the internal work, respectively. We used 0.2 as the Poisson's ratio, appropriate for monzonite (e.g., *Kulhawy*, 1975). Changing 1) the DVC parameters, 2) threshold strain used to calculate ∂W_{fric} and ∂W_{int}, and 3) elastic moduli used to calculate ∂W_{int}, from 10-50 MPa, did not change the main results of the energy budget analysis, (Figures S2-3) discussed in detail in the next section.

3. Results

3.1. Four-dimensional displacement and strain fields

The differing roughness of the preexisting faults produced contrasting failure behavior (Figure 3). Figure 3 shows slices of the incremental 3D displacement fields parallel and perpendicular to the fault strike in both experiments. The cumulative applied axial displacement, u_z, increases downward. The total magnitude of u_z depends on how the core was mounted into the deformation apparatus, and so is not physically significant. Note, the u_z of the first scan differs in each experiment (Figure 2). The smoother fault (Figure 3A) slid continuously throughout the experiment. In contrast, the rougher fault (Figure 3B) slid continuously initially, but then became locked, and caused the upper block (hanging wall) of the core to fracture. Following failure of the upper block, the lower block then failed.

The incremental displacement fields calculated from DVC analysis provide insights into deformation as the faults slid, and the blocks failed. Slices of the displacement fields at the center of the cores, both parallel and perpendicular to the fault, reveal critical differences between the experiments (Figure 3). Whereas negligible displacement occurred within the lower block of the smoother fault experiment, displacements of up to 50% of the applied axial displacement (50 µm) occurred within the lower block of the rougher fault experiment. Furthermore, the directions of these displacement vectors were primarily perpendicular to σ_1 (horizontal). The rougher fault interface enhanced coupling of the fault interfaces, leading to displacement perpendicular to σ_1 within the lower block.

These displacement fields also reveal differences in down-dip slip between the experiments (Figure 3). Parallel to the smoother fault, the upper block moved both downward and horizontally with similar magnitudes. In contrast, slip on the rougher fault produced horizontal displacements in the upper block that were less than 10% of the vertical displacements. The smoother fault allowed both dip-slip and strike-slip motion of similar magnitudes, whereas the rougher fault only accommodated significant dip-slip. Movies S1-2 show the complete evolution of these displacement field slices throughout both experiments.

In some of the fault-parallel displacement field slices, the fault plane does not appear as a perfectly horizontal line. In particular, this intersection of the fault plane with a vertical fault strike-parallel plane appears to have a slightly positive and negative slope in the experiments with the smoother and rougher faults, respectively. This appearance reflects the coupling of the core surfaces across the fault, producing a gradation in the displacement vectors across the fault plane, as well as the minor curvature of the fault interfaces near the edges of the cores.

To examine off-fault deformation and strain localization surrounding the faults, we now focus on the distribution of strain perpendicular to the fault surface. To probe this strain distribution, we built median projections of the 3D strain fields within a central, fault-perpendicular 2 mm-thick slab (Figure 4). We examined the normal fault-perpendicular horizontal strain, ε_{xx}, normal vertical strain, ε_{zz}, and the magnitude of shear strain, $|\varepsilon_{xz}|$. We also used this slab, and the resulting median projections of the displacement and strain fields, to calculate the components of the energy budget. Dilatational strain is considered negative in the adopted sign convention.

Characteristic examples of strain field projections from both experiments highlight that the smoother fault produced more localized distributions of strain than the rougher fault (Figure 4). Movies S3-4 show the complete evolution of these strain projections throughout both experiments. The magnitudes of strains within the smoother fault core were higher than the magnitudes within the rougher fault: note the differing scale bar limits for the strain magnitudes. In addition, the rougher fault inhibited the localization of ε_{xx} more significantly than the other strain components, ε_{zz} and ε_{xz}.

The strain field projections show that some segments of each fault host differing magnitudes of incremental normal and shear strains than other segments of the fault (Figure 4). Despite the overall planarity of the fault surfaces, localizations of lower and higher strain magnitudes develop along the fault. Volumes with lower strain may reflect the interlocking of asperities that restrict movement across and along the fault plane.

3.2. Strain localization surrounding sliding faults

To quantify the evolving distribution of strain, we sampled the median projections (i.e., Figure 4) of the strain field with transects. Figure 5 shows a characteristic example of this sampling technique for one DVC incremental strain field of one experiment. We sampled the strain components along fault-perpendicular transects that traverse the length of the fault (Figure 5). Movies S5-6 show the full evolution of this approach to strain sampling throughout both experiments. This technique enables examining the distribution of strain both along and across the fault. In this example DVC increment, high values of ε_{xx} along the fault do not coincide with high values of ε_{zz}, while the distribution of high values of ε_{xz} is relatively consistent along the fault. The strains sampled along the transects (i.e., across the fault) show that the distribution of high values of ε_{xx}, ε_{zz}, and ε_{xz} were relatively symmetric across the fault in this increment of the experiment.

To compare the evolving across-fault strain distributions revealed in these transects throughout both experiments, we built an averaged transect for each DVC increment of each experiment. We report the mean of the strains in the central five transects (light blue to green lines in Figure 5) at the same along-transect distances. We focus on only these central transects in order to avoid artefacts near the core edges.

These averaged transects (Figure 6) confirm and quantify the qualitative observations of the median strain projections shown in Figure 4 and Movies S5-6. The smoother fault localized strains into smaller volumes, and produced higher strains within the fault zone compared to the rougher fault (Figure 6). The rougher fault produced higher strains in the upper block, producing an asymmetry to the damage zone. This asymmetry contrasts with the generally symmetrical strain distribution across the smoother fault.

From the five central transects that are averaged to produce one curve in Figure 6, we track the width of the zones that host higher strains, which we consider indicative of the fault zones. These evolving widths indicate how the thickness of the fault zone changes, as quantified by the three independent 2D strain components. The precise thickness determined with this method may overestimate the true fault zone thickness because the spatial resolution of the DVC analysis, and subsequent median filtering, limit the minimum detected thickness. The red horizontal lines in Figure 7 show this limit. For each of these set of transects in each DVC increment, we found the width of the transect that hosts strains >25%, >50% and >75% of the maximum strain of that transect. We report the mean and standard deviation of these high strain zone widths from the five transects (Figure 7).

The smoother fault produced narrower high strain zones (<0.5 mm for strains >25% of the maximum strain) than the rougher fault (1-3 mm) (Figure 7). In both experiments, the strains >75% of the maximum strain localized to volumes close to the spatial resolution of the DVC analysis (20 voxels, 0.13 mm). After 1000 μm of applied axial displacement along the smoother fault, the width of the high normal strain zones (ε_{xx} and ε_{zz}) and high ε_{xz} zone began to increase. Slip along the rougher fault also increased the width of high ε_{zz} and ε_{xz}. In contrast, the high ε_{xx} zone did not increase in width in this experiment. Sliding on the rougher fault created higher magnitudes of off-fault deformation than the smoother fault, producing varying high strain zone widths. Both faults produced wider fault zones of elevated ε_{zz} and ε_{xz} with continued applied displacement, but only the smoother fault produced increasing wide zones of ε_{xx}.

3.3. Energy budget partitioning

Tracking the incremental components of the energy budget throughout each experiment reveals that the work done in internal deformation of the host rock in each sliding step of the experiment, ∂W_{int}, was generally 5-20% of the total work done on the system within these steps, ∂W_{ext} (Figure 8). The incremental work done against frictional slip, ∂W_{fric}, dominated the energy budget throughout each experiment, consuming generally at least 20-60% of ∂W_{ext} in both experiments, and up to nearly 100% in the experiment with the rougher fault. As the damage zone surrounding the smoother fault thickened, the percentage of ∂W_{fric} increased from 20% to 90%. The less systematic increase in the damage zone thickness of the rougher fault (Figure 7b) promoted a smaller increase in ∂W_{fric} throughout the experiment, from 60% to 90%, with the exception of four larger slip events that produced near 100% of ∂W_{ext}. Similar to ∂W_{fric}, the percentage of ∂W_{int} increased with fault slip as increasing magnitudes of stress and strain permeated the host rock surrounding the faults. The rougher fault produced a larger increase in the percentage of ∂W_{int} than the smoother fault because higher magnitudes of off-fault strain developed in the rougher fault experiment (Figures 4-6).

The percentage of ∂W_{int} relative to ∂W_{ext} was consistently smaller in the rougher fault experiment (5-20%) than the smoother fault experiment (10-40%). Accordingly, the percentage of ∂W_{fric} was generally larger in the rougher fault experiment (70-100%) than the smoother fault experiment (20-90%). These relationships reveal the interplay of ∂W_{int} and ∂W_{fric}: if less of the total work is expended in frictional slip, then relatively more work can deform the surrounding host rock.

The magnitude of external work depends on the system size and applied confining stress and differential stress. The higher confining stress and range of differential stress in the rougher fault experiment contributed to the higher external work in increments of this experiment compared to the smoother fault experiment. In addition, the higher frictional resistance of the rougher fault also likely increased the external work relative to the smoother fault. However, the applied axial displacement loading conditions of these experiments prevent equal applications of incremental external work throughout both experiments.

The magnitude of internal work depends on system size and damage zone width because ∂W_{int} is the volume integral of the strain energy density field of the off-fault volume. The smoother fault produced narrower detected on-fault volumes (Movie S3) than the rougher fault (Movie S4), and thus larger off-fault volumes. Consequently, the smoother fault generally produced larger percentages of ∂W_{int} out of total ∂W_{ext} than the rougher fault. However, the rougher fault produced higher spatially-averaged ∂W_{int} values (0.021 mJ in each 0.1^2 mm^2 square of the system) than the smoother fault (0.003 mJ in each 0.1^2 mm^2 square) (Figure 9a), as expected from the off-fault strain magnitudes (Figure 3).

The consistency of the magnitude of fault slip differed between the experiments (Figure 9b). The standard deviation in average fault slip throughout the rougher fault experiment (22 μm) is nearly four times larger than that of the smoother fault (6 μm). The greater deviation in slip along the rougher fault compared to the consistency of slip along the smoother fault captures the stick-slip-like behavior of the rougher fault, and the creep-like behavior of the smoother fault.

Although the rougher fault produces greater changes in slip than the smoother fault, the average slip magnitude is similar between the two experiments. This similarity highlights that the higher ∂W_{fric} produced by the rougher fault arises from the higher applied confining stress and differential stress in this experiment relative to the smoother fault experiment.

The largest peaks in fault slip observed in the rougher fault experiment coincide with peaks in ∂W_{int}, ∂W_{fric}, and ∂W_{ext} (Figure 2, Figure 8-9). When more work is input into the system, more strain may be done in off-fault deformation, and more fault can slip occur. This dependence of the magnitude of the energy budget components on ∂W_{ext} highlights the importance of calculating the percentage of each component out of ∂W_{ext}, rather than relying on the magnitude alone, and in tracking these percentages as individual faults slip, and fault architecture develops.

In most of the experimental increments, the sum of ∂W_{int} and ∂W_{fric} overlap ∂W_{ext}. This agreement supports the accuracy of the DVC analysis of the tomograms, and the formulations of each energy budget component. In the smoother fault experiment, 11 of the total 33 incremental energy budgets have ∂W_{ext} that do not match $\partial W_{int} + \partial W_{fric}$. In this experiment, the experiment in which the budgets do not exactly balance occur in the early stages when the core experiences relatively large displacements relative to the piston as it settles to a more vertical orientation (Movie S1). These larger displacements relative to the pistons, but not across the fault plane, tend to increase the apparent ∂W_{ext} without increasing the ∂W_{fric} or ∂W_{int} by similar magnitudes. In the rougher fault experiment, only 4 of 20 increments have this mismatch. Similar to the smoother fault experiment, these experiment increments correspond to increments with larger than typical displacements. Consequently, we suspect that the imbalance of the incremental work budgets in these few experiment increments arises from inaccuracies in the calculated DVC displacements, which increase with larger displacements.

4. Discussion

4.1. Asymmetric damage zone growth with fault slip

These experiments provide unique access to the evolving distribution of strain surrounding sliding faults, as well as the evolving components of the energy budget. The differing roughness of the precut faults influenced the macroscopic sliding and subsequent failure behavior of the monzonite cores. The smoother fault slid continuously throughout the experiment. The rougher fault initially slid, but then the upper block, and later the lower block, failed. Two other experiments performed to assess the reproducibility of these results follow the trend found in the two experiments analyzed in depth here.

Displacement fields calculated through DVC analysis reveal that the smoother fault allowed the upper block to move in both strike-slip and dip-slip motion, but the rougher fault only accommodated significant dip-slip motion (Figure 3). These restrictions produced localized ε_{xx} along the smoother fault, and more distributed ε_{xx} surrounding the rougher fault (Figure 4). Transects of the strain components perpendicular to the fault surface reveal that the smoother fault produced more localized and higher strains than the rougher fault (Figure 6). These transects highlight the asymmetry of the damage zone surrounding the rougher fault.

Such asymmetry in damage zone structure has been observed in the field (e.g., *Berg & Skar*, 2005; *Shipton et al*., 2006b; *Riley et al*., 2010; *Choi et al*., 2016). Here we were able to observe the temporal development of an asymmetric damage zone, and not only the static glimpses provided in the field. The asymmetry may have developed within the top block rather than the lower block because the top block was in contact with the moving piston. Although both blocks were not fixed and free to move under the applied axial displacement and confining stress, the top block was in direct contact with the moving piston.

We observed this asymmetric development within the same material. Numerical models suggest that asymmetric damage zone growth is promoted in tectonic environments in which a fault separates crustal materials of differing stiffness (*Ben-Zion & Shi*, 2005). In contrast, homogeneous numerical models suggest seismic ruptures propagate symmetrically and bilaterally in homogeneous material, producing symmetric damage zones (e.g., *Dalguer et al*., 2003). Differing stress conditions across and along faults are also thought to promote asymmetric damage zone development (e.g., *Choi et al*., 2016 and references therein). Here, we show that higher strains can preferentially localize on one side of a fault zone, and so produce an asymmetric damage distribution within a homogeneous crystalline material that initially hosts similar macroscopic stress fields on either side of the fault. Rougher fault surfaces promote asymmetric damage zone development by concentrating tensile stresses that promote opening-mode failure and fracture propagation to a greater degree than smoother fault surfaces.

Tracking the width of the high strain zones perpendicular to the fault surface indicates that the width of fault zones can evolve over a few millimeters of slip (Figure 7). Slip along the faults increased the damage zone widths as recognized by high axial (vertical) contraction and shear strain. However, slip along the smoother fault also increased the width of the high horizontal contraction, whereas slip along the rougher fault did not produce this trend.

The observed trend of increasing high strain zone width with slip is consistent with field observations of increasing damage zone width with fault throw or displacement (e.g., *Shipton & Cowie*, 2001; *Mitchell & Faulkner*, 2009; *Faulkner et al*., 2011; *Savage & Brodsky*, 2011). Field analyses often track the extent of damage zones using densities of microfractures (e.g., *Faulkner et al*., 2011). Our new experimental observations show that the volume of rock experiencing higher normal and shear strains near the fault core can also increase in extent with fault slip, depending on the fault roughness.

4.2. Fault roughness controls slip behavior

The evolution of the frictional work, and corresponding average slip along the faults (Figure 9), captures the differing slip behaviors observed in the two experiments. Whereas the rougher fault tended to slip in episodic events, with alternating larger and smaller slip, the smoother fault had more continuous, monotonic slip (Figure 9B). This behavior is consistent with the influence of roughness on the transition from stable to unstable slip. Rougher surfaces produce higher static normal stress concentrations between slip events than smoother surfaces. Moreover, slip events on rougher surfaces tend to produce greater changes in real contact area than events on smoother surfaces, thereby changing the frictional strength more abruptly, and promoting unstable behavior. Our *in situ* observations indicate that rougher (higher friction) materials produce episodic slip events analogous to earthquakes, while smoother (lower friction) materials produce smaller slip events of similar magnitudes that produce acoustic energy below the field detection limit.

The rougher fault experiment demonstrates that slip can evolve in precut faults that lack preexisting fault gouge (Figure 9). Except for one larger slip event, the slip magnitudes were relatively constant early in the experiment, but then became increasingly episodic with continued applied axial displacement until the intact rock surrounding the fault failed. This evolving slip behavior demonstrates the importance of the temporal history of the fault, and the accumulated real contact time, and not only the initial intact rock material properties and fault geometry.

The effective normal stress on the faults likely also influenced the transition from stable to unstable slip. Decreasing normal stress can promote unstable slip behavior (e.g., *Scholz et al.*, 1972). However, our experiments show the opposite trend: unstable slip developed in the experiment with higher confining and differential stress. The influence of roughness on slip behavior was more significant than the influence of confining stress under the ranges of confining stress and roughness captured in our experiments.

4.3. Crustal energy budget partitioning

During rupture, released elastic strain energy is partitioned into acoustic energy, frictional energy, and the energy consumed in the production of new fracture surfaces, or fracture energy (e.g., *Lockner et al*., 1991; *Shipton et al*., 2006a). Recent work has highlighted the significance of fracture energy in the coseismic energy budget as it may be comparable to or exceed the frictional energy in some scenarios (*Reches & Dewers*, 2005; *Passelègue et al*., 2016; *Nielsen et al*., 2016). Some studies suggest that discrepancies in estimates of fracture energy in crustal and laboratory earthquakes may arise from the production of off-fault damage during large crustal earthquakes (*Nielsen et al*., 2016). However, other energy budget analyses do not identify this discrepancy (*Passelègue et al*., 2016).

Here, we did not focus on the fracture energy, or W_{prop}, because the required segmentation of the experiment tomograms is the focus of a forthcoming analysis. The agreement of W_{ext} and the sum of W_{fric} and W_{int} throughout >70% of the analyzed energy budgets suggests that W_{prop} comprised a small portion of the energy budget. Throughout the final increments of the rougher fault experiment when fractures begin to propagate within the host rock, W_{prop} consumes increasing portions of the budget than earlier in the experiment. In the final one or two increments of this experiment, our calculations of W_{int} are likely overestimates because the effective elastic modulus may be lower than the prescribed 10 MPa, which reflects the elastic modulus when the monzonite begins to yield, but not immediately preceding failure. This overestimated portion of the energy budget is likely consumed as W_{prop}, rather than W_{int}.

We tracked the evolution of the energy budget throughout stable slip increments (Figure 2) that did not include flash heating and melting, thermal pressurization or other processes that decrease the effective friction with slip. During seismic slip, the production of new fracture surfaces may consume a larger portion of the energy budget than frictional slip because shear stress on the fault may decrease during slip, decreasing the coseismic frictional work. Furthermore, during rupture high, but transient, concentrations of stress and strain develop at geometric complexities along the fault, increasing the work expended to create new fracture surfaces.

Our energy budget analysis of aseismic slip events demonstrates that the energy expended in off-fault deformation comprises generally 5-20% of the total energy budget. The energy expended against frictional slip dominates the deformational energy budget, consuming generally 50-100% of the total budget. This low estimate of W_{int} is consistent with previous estimates of internal work in physical dry sand experiments of contracting accretionary wedges (*McBeck et al*., 2018a), and in analyses that neglect the contribution of W_{int} to the overall energy budget (*Gutscher et al*., 1998; *Burbidge & Braun*, 2002; *Yagupsky et al*., 2014). Estimates of W_{int} from linear elastic models may comprise a larger portion of the energy budget (e.g., *Savage & Cooke*, 2010; *Newman & Griffith*, 2014; *Madden et al*., 2017) because numerical complexities near fault tips and geometric irregularities can produce unrealistically high stresses and strains.

The dominance of frictional work in our and previous energy budget analyses suggests that field geologists may only need to constrain the energy consumed in frictional slip in order to assess the overall energetics of crustal systems. This simplification may enable robust field predictions of fault development and interaction based only on estimates of frictional work. However, we emphasize that W_{int} consumes a non-negligible portion of the total energy budget in these systems with precut, slipping faults. In tectonic systems that lack km-scale faults, or host only smaller segmented systems, the portion of the total energy budget consumed in W_{int} may exceed 5-20%.

Frictional work depends on the slip and shear tractions along faults, and so we expect differing magnitudes of frictional work in tectonic environments and experiments with differing lithostatic stresses. Slip on the smoother and rougher faults in our experiments produce on average 1 MJ/m^2 and 5 MJ/m^2 of frictional work normalized by fault area, respectively. This range in frictional work is comparable with previous estimates: 2-3 MJ/m^2 (*Reches & Dewers*, 2005), and 6-7 MJ/m^2 (*Coffey et al*., 2019), exceeds other estimates (500-1000 J/m^2) (*Passelègue et al*., 2016) and is lower than other estimates: 19-51 MJ/m^2 (*Fulton et al*., 2013) and 105-228 MJ/m^2 (*Savage et al*., 2014). These differences likely arise in part from the differing confining stresses and/or effectiveness of processes that reduce fault strength during seismic slip. Because both frictional work and the total energy input into the system are functions of normal stress, future studies should endeavor to estimate the percentage of the total energy input consumed by frictional work. This percentage provides additional insight into the energetic importance of frictional slip than the magnitude of work normalized by fault area. Furthermore, our contribution demonstrates that as fault zones thicken with slip, the rate at which they consume frictional work out of the total energy input increases. Our results demonstrate the temporal variability of components of the energy budget within and surrounding sliding faults, and that fault zone thickness influences frictional work. In crustal tectonic environments, the damage zones surrounding faults may saturate to a steady-state thickness, or continue to increase with slip (e.g., *Faulkner et al*., 2011; *Savage & Brodsky*, 2011). If damage zones saturate to a constant thickness, then estimates of frictional work produced in one seismic event along one fault will be comparable to estimates of frictional work from a subsequent earthquake on the same fault. However, these frictional work estimates may not be comparable if the damage zone width increases.

5. Conclusions

To investigate strain localization produced by slipping faults, and the resulting energetics of on- and off-fault deformation, we slid two precut faults with different roughness between intact crystalline rock inside the HADES triaxial deformation apparatus while acquiring *in situ* X-ray microtomograms. Using displacement fields calculated from digital volume correlation analysis, we tracked the evolution of the energy budget throughout both experiments. These energy budget evolutions enable quantitative comparisons of the amount of off-fault deformation and strain within the fault zones. Throughout both experiments, the energy expended in off-fault deformation comprised 5-20% of the total energy budget, while the energy expended against frictional slip comprised 50-100% of the total budget. Our novel representation and sampling of the strain tensor field surrounding the faults reveal that the thickness of the high strain zone produced by faults can evolve over a few millimeters of slip. This unique monitoring also reveals that asymmetric damage zones can develop across faults embedded in the same host rock over these small, stable increments of slip. Furthermore, the episodic nature of fault slip can evolve through time along the same fault, and thus is dependent on the deformation history of the fault and surrounding crust.

Acknowledgements

The deformation apparatus was built by Sanchez Technology. Elodie Boller, Paul Tafforeau, and Alexander Rack provided advice on the design of the tomography setup. Stephen Hall and Erika Tudisco provided advice on the application of TomoWarp2. This study received funding from the Norwegian Research Council (project HADES, grant 250661). Beamtime was allocated at the European Synchrotron Radiation Facility (Long Term Proposal ES-295). Data storage was provided by UNINETT Sigma2 - the National Infrastructure for High Performance Computing and Data Storage in Norway (project NS9073K). We thank Editor

Takeshita, Heather Savage and an anonymous reviewer for suggestions that improved the manuscript.

References

Aben, F. M., Doan, M. L., Mitchell, T. M., Toussaint, R., Reuschlé, T., Fondriest, M., Gratier, J.-P. & Renard, F. (2016). Dynamic fracturing by successive coseismic loadings leads to pulverization in active fault zones. *Journal of Geophysical Research: Solid Earth*, *121*(4), 2338-2360.

Berg, S. S., Skar, T., 2005. Controls on damage zone asymmetry of a normal fault zone: outcrop analyses of a segment of the Moab fault, SE Utah. *Journal of Structural Geology*, *27*(10), 1803-1822.

Ben-Zion, Y., Sammis, C., 2003. Characterization of fault zones. *Pure and Applied Geophysics*, 160, 677–715.

Ben-Zion, Y., Shi, Z. 2005. Dynamic rupture on a material interface with spontaneous generation of plastic strain in the bulk. *Earth and Planetary Science Letters*, *236*(1-2), 486-496.

Brantut, N., Schubnel, A., Rouzaud, J. N., Brunet, F., Shimamoto, T., 2008. High-velocity frictional properties of a clay-bearing fault gouge and implications for earthquake mechanics. *Journal of Geophysical Research: Solid Earth*, *113*(B10), 113, B10401, doi:10.1029/2007JB005551.

Burbidge, D. R., Braun, J., 2002. Numerical models of the evolution of accretionary wedges and fold-and-thrust belts using the distinct-element method. *Geophysical Journal International*, *148*(3), 542-561.

Bürgmann, R., 2018. The geophysics, geology and mechanics of slow fault slip. *Earth and Planetary Science Letters*, *495*, 112-134.

Candela, T., Renard, F., Klinger, Y., Mair, K., Schmittbuhl, J. Brodsky, E., 2012. Roughness of fault surfaces over nine decades of length scales, *Journal of Geophysical Research*, 117, B08409, doi:10.1029/2011JB009041.

Carpenter, B. M., Saffer, D. M., Marone, C., 2015. Frictional properties of the active San Andreas Fault at SAFOD: Implications for fault strength and slip behavior. *Journal of Geophysical Research: Solid Earth*, *120*(7), 5273-5289.

Choi, J. H., Edwards, P., Ko, K., Kim, Y. S. (2016). Definition and classification of fault damage zones: A review and a new methodological approach. *Earth-Science Reviews*, *152*, 70-87.

Cocco, M., Spudich, P., Tinti, E., 2006. On the mechanical work absorbed on faults during earthquake ruptures. In *Radiated Energy and the Physics of Earthquakes Faulting*, AGU Monograph Series 170, Washington D.C., 237–254.

Coffey, G. L., Savage, H. M., Polissar, P. J., Rowe, C. D., & Rabinowitz, H. S. (2019). Hot on the trail: Coseismic heating on a localized structure along the Muddy Mountain fault, Nevada. *Journal of Structural Geology*, *120*, 67-79.

Collettini, C., Niemeijer, A., Viti, C., Marone, C., 2009. Fault zone fabric and fault weakness. *Nature*, *462*(7275), 907-910, doi:10.1038/nature08585.

Cooke, M. L., Madden, E. H., 2014. Is the Earth lazy? A review of work minimization in fault evolution. *Journal of Structural Geology*, *66*, 334-346.

Dalguer, L. A., Irikura, K., Riera, J. D., 2003. Simulation of tensile crack generation by three-dimensional dynamic shear rupture propagation during an earthquake. *Journal of Geophysical Research: Solid Earth*, *108*(B3), 2144, doi:10.1029/2001JB001738.

Del Castello, M., Cooke, M.L., 2007. Underthrusting-accretion cycle: work budget as revealed by the boundary element method, *Journal of Geophysical Research: Solid Earth*, 113, B12404, 1–14, doi:10.1029/2007JB004997.

Du, Y., Aydin, A., 1993. The maximum distortional strain energy density criterion for shear fracture propagation with applications to the growth paths of enechelon faults. *Geophysical Research Letters*, *20*(11), 1091-1094.

Faulkner, D. R., Mitchell, T. M., Jensen, E., Cembrano, J., 2011. Scaling of fault damage zones with displacement and the implications for fault growth processes. *Journal of Geophysical Research: Solid Earth*, *116*(B5), 116, B05403, doi:10.1029/2010JB007788.

Fulton, P. M., Brodsky, E. E., Kano, Y., Mori, J., Chester, F., Ishikawa, T., Harris, R., Lin, W., Eguchi, N., Toczko, S., 2013. Low coseismic friction on the Tohoku-Oki fault determined from temperature measurements. *Science*, *342*(6163), 1214-1217.

Giorgetti, C., Tesei, T., Scuderi, M., Collettini, C., 2019. Fault Reactivation in Gouge-filled Fault Zones: Experimental Insights. Accepted pending revisions in *Journal of Geophysical Research: Solid Earth.*

Griffith, W. A., Nielsen, S., Di Toro, G., Smith, S. A., 2010. Rough faults, distributed weakening, and off-fault deformation. *Journal of Geophysical Research: Solid Earth*, *115*(B8), doi:10.1029/2009JB006925.

Gutscher, M. A., Kukowski, N., Malavieille, J., Lallemand, S., 1998. Episodic imbricate thrusting and underthrusting: Analog experiments and mechanical analysis applied to the Alaskan accretionary wedge. *Journal of Geophysical Research: Solid Earth*, *103*(B5), 10161-10176.

Ikari, M. J., Saffer, D. M., Marone, C., 2009. Frictional and hydrologic properties of a major splay fault system, Nankai subduction zone. *Geophysical Research Letters*, *36*(20), 36, L20313, doi:10.1029/2009GL040009.

Kaduri, M., Gratier, J.-P., Renard, F., Çakir, Z., Lasserre, C., 2017. The implications of fault zone transformation on aseismic creep: Example of the North Anatolian Fault, Turkey. *Journal of Geophysical Research: Solid Earth*, 122, 4208–4236, doi:10.1002/ 2016JB013803.

Katz, O., Z. Reches, 2004. Microfracturing, damage, and failure of brittle granites, *Journal of Geophysical Research: Solid Earth*, 109, B01206, doi:10.1029/2002JB001961.

Kulhawy, F. H., 1975. Stress deformation properties of rock and rock discontinuities. *Engineering Geology*, *9*(4), 327-350.

Lockner, D., Byerlee, J. D., Kuksenko, V., Ponomarev, A., Sidorin, A., 1991. Quasi-static fault growth and shear fracture energy in granite. *Nature*, *350*(6313), 39.

Ma, K. F., Tanaka, H., Song, S. R., Wang, C. Y., Hung, J. H., Tsai, Y. B., Mori, J., Song, Y.F, Yeh, E.C., Soh, W., Sone, H., 2006. Slip zone and energetics of a large earthquake from the Taiwan Chelungpu-fault Drilling Project. *Nature*, *444*(7118), 473-476, doi:10.1038/nature05253.

Madden, E. H., Cooke, M. L., McBeck, J., 2017. Energy budget and propagation of faults via shearing and opening using work optimization. *Journal of Geophysical Research: Solid Earth*, *122*(8), 6757-6772.

McBeck, J., Cooke, M., Souloumiac, P., Maillot, B., Mary, B., 2018a. The influence of detachment strength on the evolving deformational energy budget of physical accretionary prisms. *Solid Earth*, *9*, 1421–1436, doi:10.5194/se-9-1421-2018.

McBeck, J., Kobchenko, M., Hall, S. A., Tudisco, E., Cordonnier, B., Meakin, P., Renard, F., 2018b. Investigating the onset of strain localization within anisotropic shale using digital volume correlation of time-resolved X-ray microtomography images. *Journal of Geophysical Research: Solid Earth*, doi:10.1029/2018JB015676.

Milliner, C. W., Dolan, J. F., Hollingsworth, J., Leprince, S., Ayoub, F., Sammis, C. G., 2015. Quantifying near-field and off-fault deformation patterns of the 1992 Mw 7.3 Landers earthquake. *Geochemistry, Geophysics, Geosystems*, *16*(5), 1577-1598.

Mitchell, T. M., Faulkner, D. R., 2009. The nature and origin of off-fault damage surrounding strike-slip fault zones with a wide range of displacements: A field study from the Atacama fault system, northern Chile. *Journal of Structural Geology*, *31*(8), 802-816.

Mitra, G., Boyer, S. E., 1986. Energy balance and deformation mechanisms of duplexes. *Journal of Structural Geology*, *8*(3-4), 291-304.

Newman, P. J., Griffith, W. A, 2014. The work budget of rough faults. *Tectonophysics*, 636, 100-110.

Nielsen, S., Spagnuolo, E., Violay, M., Smith, S., Di Toro, G., Bistacchi, A., 2016. G: Fracture energy, friction and dissipation in earthquakes. *Journal of Seismology*, *20*(4), 1187-1205.

Okubo, C. H., Schultz, R. A., 2005. Evolution of damage zone geometry and intensity in porous sandstone: insight gained from strain energy density. *Journal of the Geological Society*, *162*(6), 939-949.

Passelègue, F., Schubnel, A., Nielsen, S., Bhat, H. S., Deldicque, D., Madariaga, R., 2016. Dynamic rupture processes inferred from laboratory microearthquakes. *Journal of Geophysical Research: Solid Earth*, *121*(6), 4343-4365.

Pittarello, L., Di Toro, G., Bizzarri, A., Pennacchioni, G., Hadizadeh, J., Cocco, M., 2008. Energy partitioning during seismic slip in pseudotachylyte-bearing faults (Gole Larghe Fault, Adamello, Italy). *Earth and Planetary Science Letters*, *269*(1-2), 131-139.

Reches, Z. E., Dewers, T. A., 2005. Gouge formation by dynamic pulverization during earthquake rupture. *Earth and Planetary Science Letters*, *235*(1-2), 361-374.

Renard, F., Cordonnier, B., Dysthe, D. K., Boller, E., Tafforeau, P., Rack, A., 2016. A deformation rig for synchrotron microtomography studies of geomaterials under conditions down to 10 km depth in the Earth. *Journal of Synchrotron Radiation*, 23(4), 1030-1034.

Renard, F., Cordonnier, B., Kobchenko, M., Kandula, N., Weiss, J., Zhu, W., 2017. Microscale characterization of rupture nucleation unravels precursors to faulting in rocks. *Earth and Planetary Science Letters*, *476*, 69-78.

Renard, F., McBeck, J., Cordonnier, B., Zheng, X., Kandula, N., Sanchez, J. R., Kobchenko, M., Noiriel, C., Zhu, W., Meakin, P., Fusseis, F., 2018a. Dynamic In Situ Three-Dimensional Imaging and Digital Volume Correlation Analysis to Quantify Strain Localization and Fracture Coalescence in Sandstone. *Pure and Applied Geophysics*, 1-33, doi:10.1007/s00024-018-2003-x.

Renard, F., Weiss, J., Mathiesen, J., Ben-Zion, Y., Kandula, N., Cordonnier, B., 2018b. Critical Evolution of Damage Toward System-Size Failure in Crystalline Rock. *Journal of Geophysical Research: Solid Earth*, *123*(2), 1969-1986, doi: 10.1002/2017JB014964.

Riley, P. R., Goodwin, L. B., Lewis, C. J., 2010. Controls on fault damage zone width, structure, and symmetry in the Bandelier Tuff, New Mexico. *Journal of Structural Geology*, *32*(6), 766-780.

Savage, H. M., & Brodsky, E. E. (2011). Collateral damage: Evolution with displacement of fracture distribution and secondary fault strands in fault damage zones. *Journal of Geophysical Research: Solid Earth*, *116*(B3).

Savage, H. M., Cooke, M. L., 2010. Unlocking the effects of friction on fault damage zones. *Journal of Structural Geology*, *32*(11), 1732-1741.

Savage, H. M., Polissar, P. J., Sheppard, R., Rowe, C. D., Brodsky, E. E., 2014. Biomarkers heat up during earthquakes: New evidence of seismic slip in the rock record. *Geology*, *42*(2), 99-102.

Scholz, C., Molnar, P., & Johnson, T. (1972). Detailed studies of frictional sliding of granite and implications for the earthquake mechanism. *Journal of geophysical research*, *77*(32), 6392-6406.

Shelef, E., Oskin, M., 2010. Deformation processes adjacent to active faults: Examples from eastern California. *Journal of Geophysical Research: Solid Earth*, 115, B05308, doi: 10.1029/2009JB006289.

Shi, Z., Ben-Zion, Y., 2006. Dynamic rupture on a bimaterial interface governed by slip-weakening friction. *Geophysical Journal International*, 165(2), 469-484.

Shipton, Z. K., Cowie, P. A., 2001. Damage zone and slip-surface evolution over μm to km scales in high-porosity Navajo sandstone, Utah. *Journal of Structural Geology*, *23*(12), 1825-1844.

Shipton, Z. K., Evans, J. P., Abercrombie, R. E., Brodsky, E. E., 2006a. The missing sinks: Slip localization in faults, damage zones, and the seismic energy budget. In Abercrombie, R. (Eds) *Earthquakes: Radiated Energy and the Physics of Faulting*, 217-222. Washington, DC: AGU.

Shipton, Z. K., Soden, A. M., Kirkpatrick, J. D., Bright, A. M., Lunn, R. J., 2006b. How thick is a fault? Fault displacement-thickness scaling revisited. In Abercrombie, R. (Eds) *Earthquakes: Radiated Energy and the Physics of Faulting*, 193-198. AGU.

Tenthorey, E., Cox, S. F., Todd, H. F., 2003. Evolution of strength recovery and permeability during fluid–rock reaction in experimental fault zones. *Earth and Planetary Science Letters*, *206*(1-2), 161-172.

Timoshenko, S.P., Goodier, J.N., 1951. Theory of Elasticity, 2nd ed. McGraw-Hill, New York.

Toy, V. G., Niemeijer, A., Renard, F., Morales, L., Wirth, R., 2017. Striation development depends on temperature under hydrothermal conditions: microstructural processes and mechanical implications, *Journal of Geophysical Research*, 122, doi:10.1002/2016JB013498.

Tudisco, E., Andò, E., Cailletaud, R., Hall, S. A., 2017. TomoWarp2: a local digital volume correlation code. *SoftwareX*, 6, 267-270.

Wesnousky, S. G., 2006. Predicting the endpoints of earthquake ruptures. *Nature*, 444, 358–360, doi:10.1038/nature0525.

Wilson, B., Dewers, T., Reches, Z. E., Brune, J., 2005. Particle size and energetics of gouge from earthquake rupture zones. *Nature*, *434*(7034), 749–752.

Yagupsky, D. L., Brooks, B. A., Whipple, K. X., Duncan, C. C., Bevis, M., 2014. Distribution of active faulting along orogenic wedges: Minimum-work models and natural analogue. *Journal of Structural Geology*, *66*, 237-247.

Figure 1

The comprehensive framework of the energy budget surrounding faults. The energy budget provides a quantitative and concise method of assessing the impact of diverse deformational processes on the overall system energetics. Friction work, W_{fric}, captures the energy expended in frictional slip along faults (red). Internal work, W_{int}, captures the energy expended in off-fault deformation (blue). External work, W_{ext}, captures the total energy input to the system (purple).

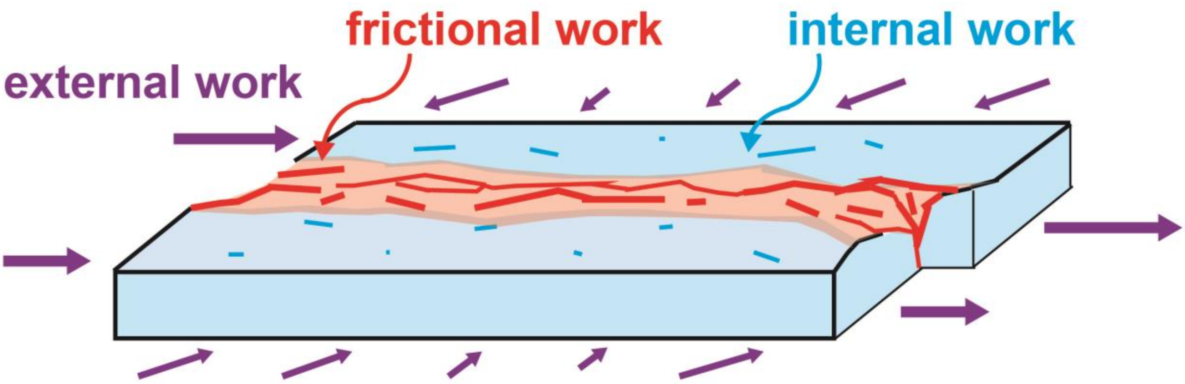

Figure 2

Schematics, example tomograms, and loading history of experiments with smoother (a, experiment M6) and rougher (b, experiment M8) preexisting fault surfaces. Tomograms are colored by density differences, which correspond to different minerals and open fractures. In the graphs, the black dots show the macroscopic differential stress and applied axial displacement, u_z, when each tomogram was acquired. Red lines show the applied axial displacement and differential stress when each tomogram used in DVC analysis was acquired. Each tomogram pair are separated by approximately 50 μm of u_z.

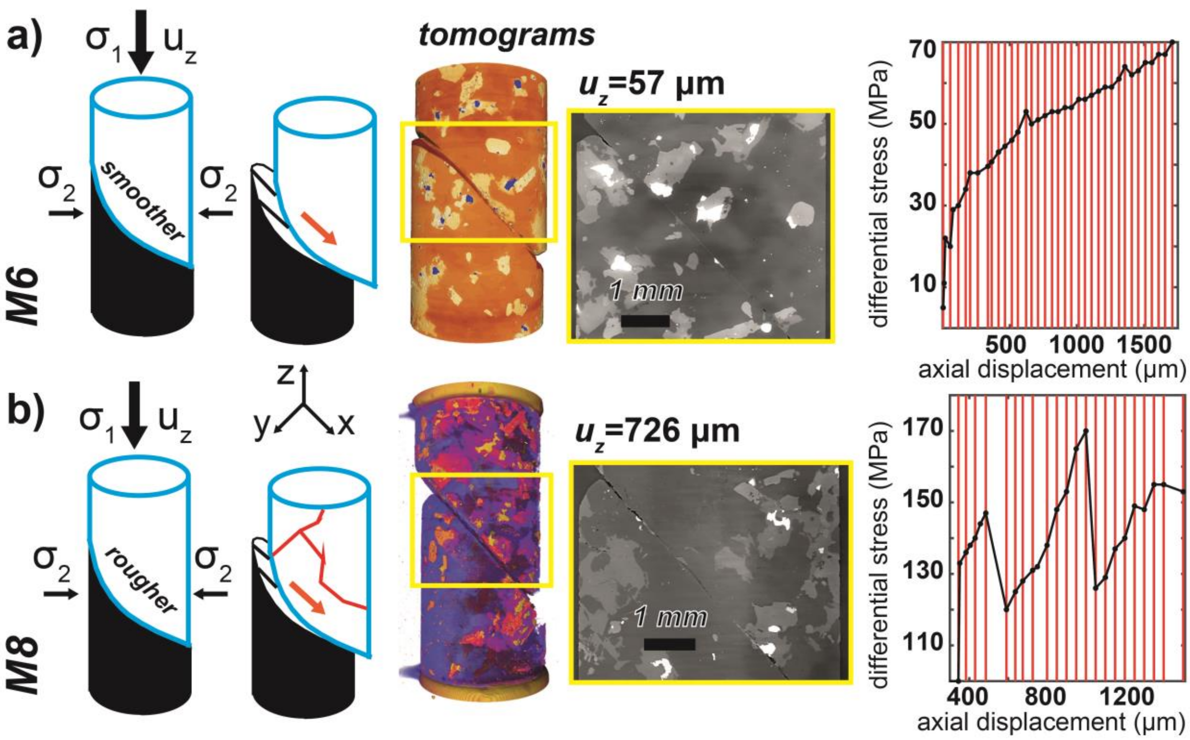

Figure 3

Slices of 3D displacement fields calculated with DVC analysis for experiments with smoother (a) and rougher (b) faults. Color indicates the magnitude of displacement vectors. Arrows indicate direction. Slices are taken from the centers of the core parallel to the *x*-axis (left) and *y*-axis (right). The preexisting fault strikes were aligned parallel and perpendicular to the horizontal axes. Numbers indicate the macroscopic axial displacement at the acquisition of the tomogram pairs used in the DVC analysis. Movies S1-2 show the complete evolution of these displacement field slices throughout both experiments.

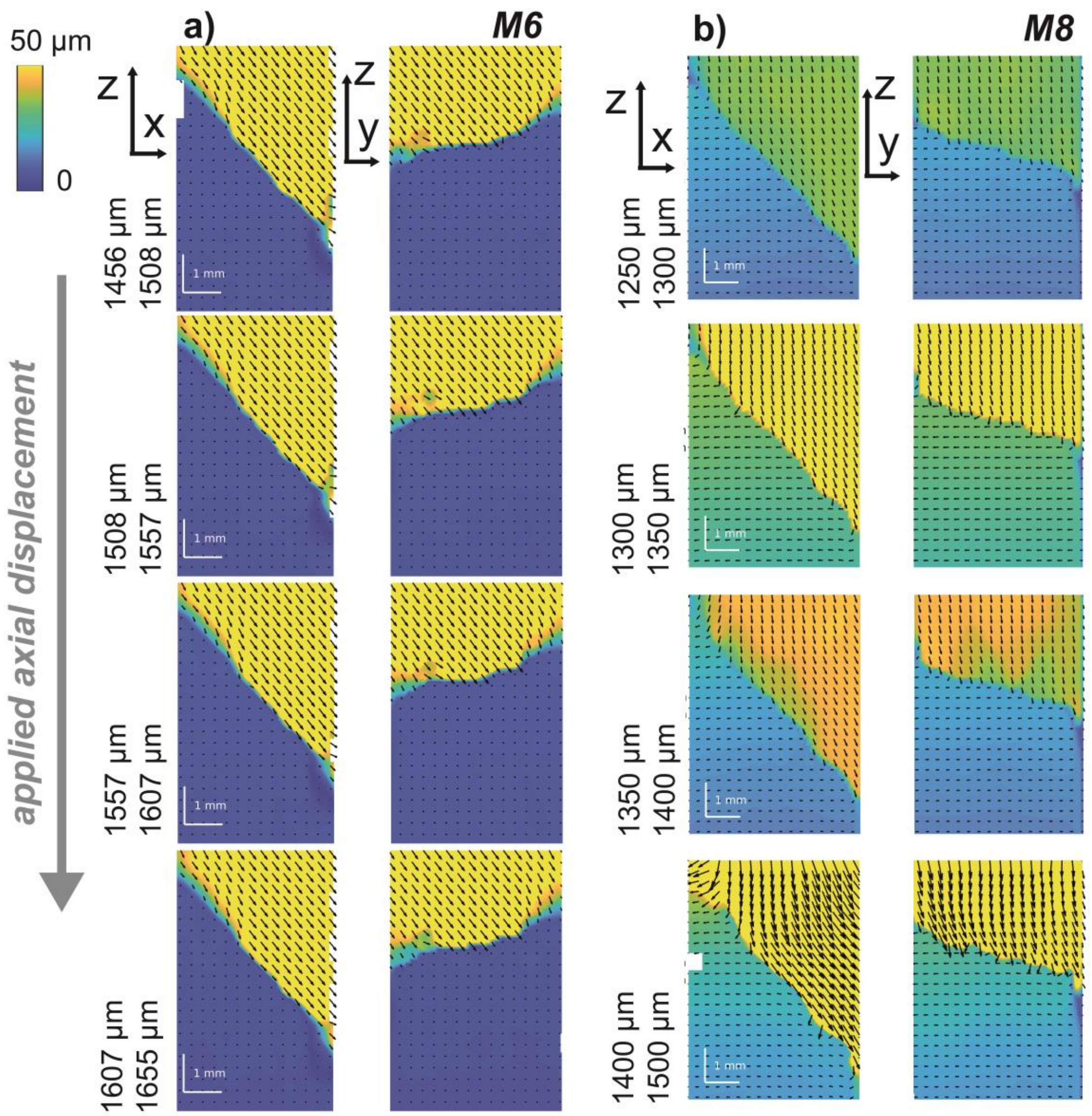

Figure 4

Median projections of 2D strain components for experiments with smoother (a) and rougher (b) faults for one increment of each experiment. Median projections are taken from strain field of the 2 mm thick fault strike-perpendicular slab at the center of the cores. Left: Normal horizontal dilation, ε_{xx}. Center: Normal vertical contraction, ε_{zz}. Right: shear strain magnitude, $|\varepsilon_{xz}|$. Dilation is negative and contraction is positive in the adopted sign convention. Note the larger magnitude color scale limits for the smoother fault experiment (M6) than the rougher fault experiment (M8). The numbers at left show the applied axial displacement at the acquisition of the tomogram pair used in the DVC calculation. Movies S3-4 show the complete evolution of these strain field projections throughout both experiments.

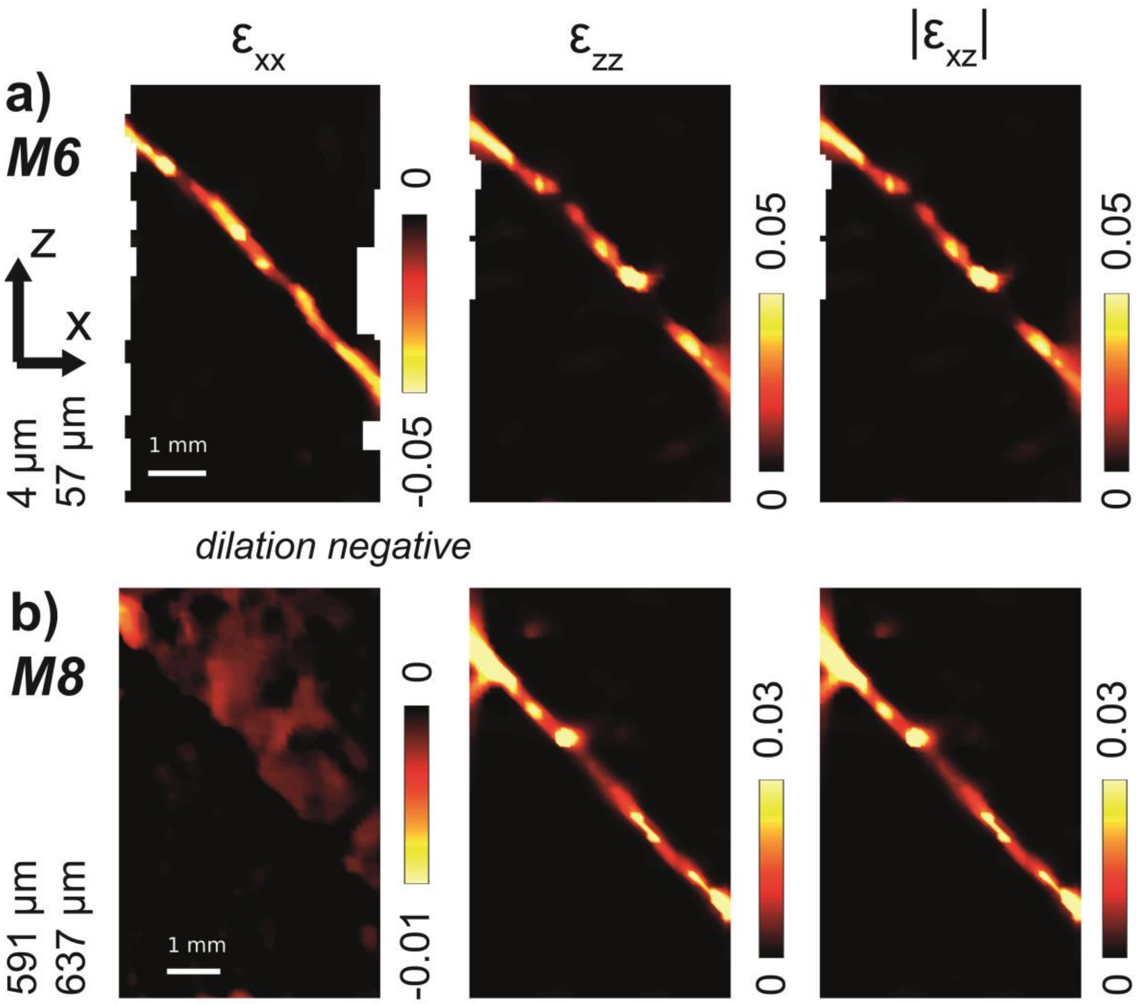

Figure 5

Method of sampling strain field with transects shown for one DVC increment of the smoother fault experiment (M6). a) Location of transects (colored lines) over example strain field. Top yellow arrow shows the position of each transect along the fault. Bottom yellow arrow shows the position of each sampling location along the transect. Transects start in the lower block, so higher positions along them are in the upper block (hanging wall). b-d) Mean of strain sampled along transect relative to transect position along fault (top row), and position along transect (bottom row). b) Normal horizontal dilation, ε_{xx}. c) Normal vertical contraction, ε_{zz}. d) Shear strain magnitude, $|\varepsilon_{xz}|$. Dilation is negative. Movies S5-6 show the full evolution of this strain sampling throughout both experiments.

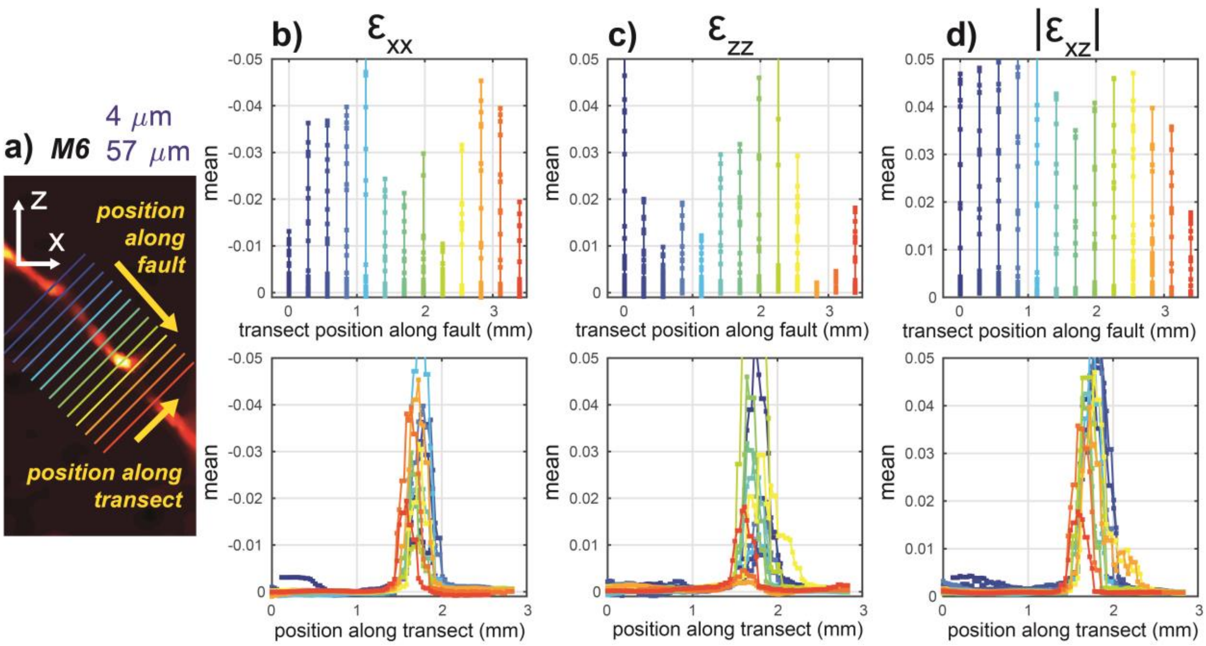

Figure 6

Complete evolution of averaged strain transects throughout experiments with smoother (top row) and rougher (bottom row) faults for (a) ε_{xx}, (b) ε_{zz}, and (c) $|\varepsilon_{xz}|$. Averaged transects were constructed by finding the mean of the strain along the 5 transects within the center of the core (light blue to green lines in Figure 5), and shown in gray area in inset of a). Color of curves indicates the macroscopic axial displacement, u_z, when the second tomogram used in the DVC analysis was acquired.

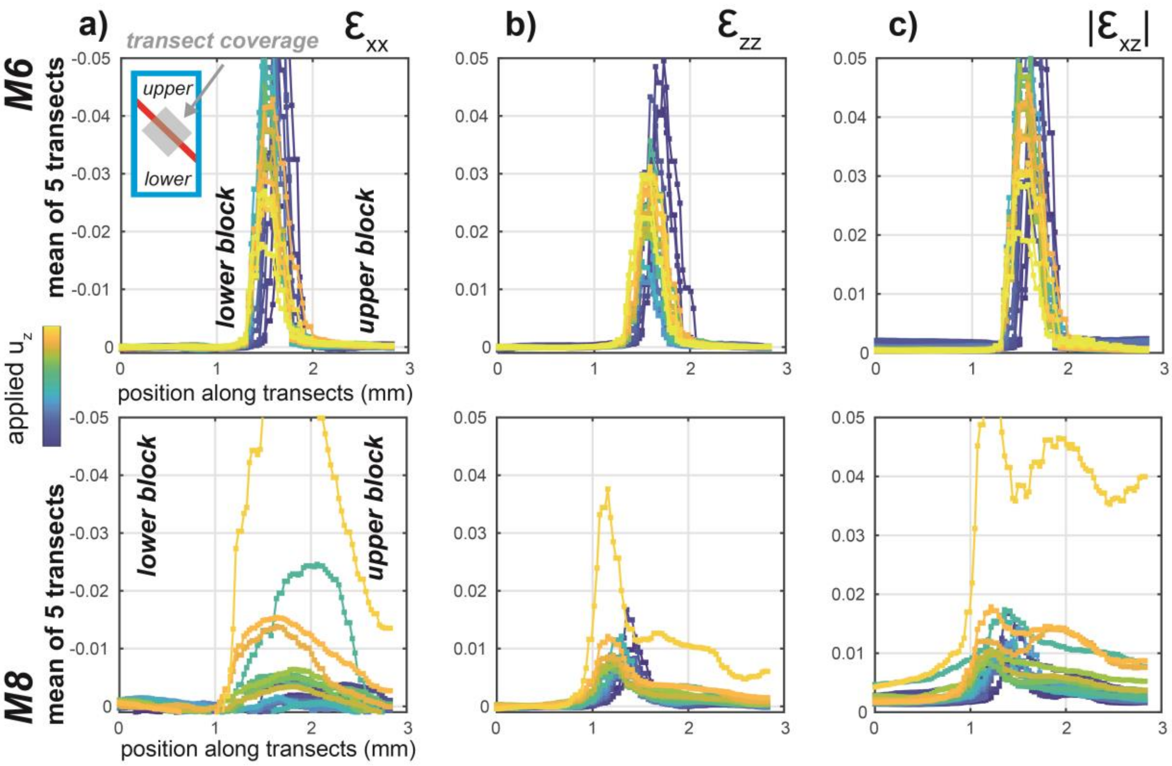

Figure 7

Evolution of fault zone width throughout experiments with smoother (upper row) and rougher (lower row) faults. Dark, medium and light gray symbols show the mean ± one standard deviation of the widths of the five central transects that exceed 25%, 50% and 75%, respectively, of the maximum strain along each transect for (a) negative ε_{xx}, (b) positive ε_{zz}, and (c) $|\varepsilon_{xz}|$. Red lines show the node spacing size used in DVC analysis (20 voxels, 0.13 mm). Gray lines show the linear best fit to means of strain zone widths for each percentage and strain component.

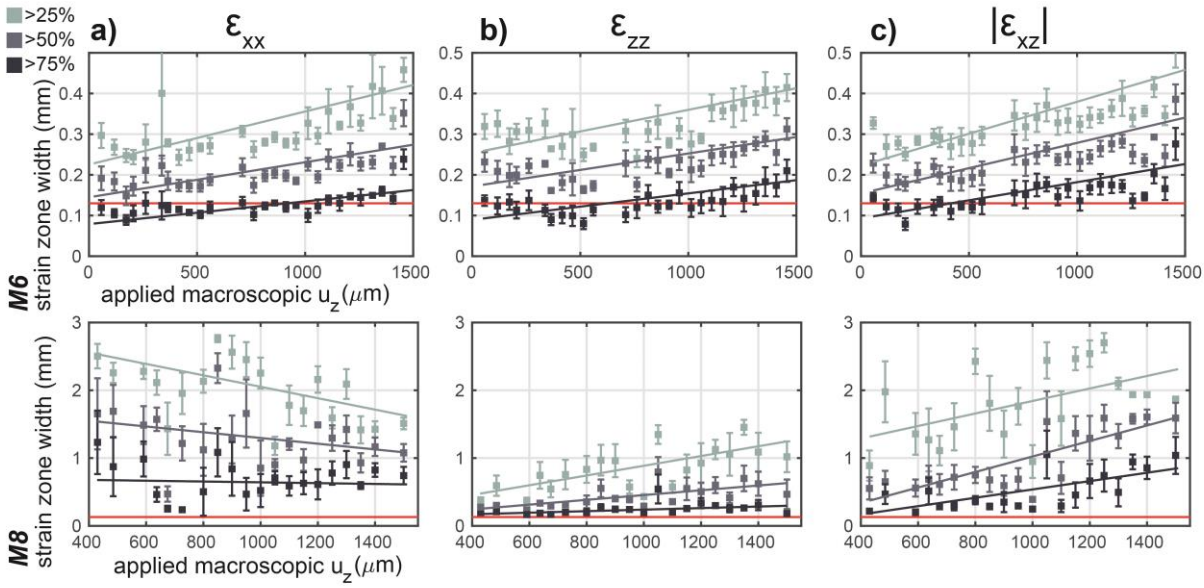

Figure 8

Evolution of the energy budget in smoother (a) and rougher (b) fault experiments. Incremental energy budget components calculated from incremental displacement and strain fields: internal work (blue), frictional work (red), frictional + internal work (pink), and external work (black). Vertical bars show the range of energy budget components derived from range of experimental measurements See Methods and Figure S1 for details on the range calculation.

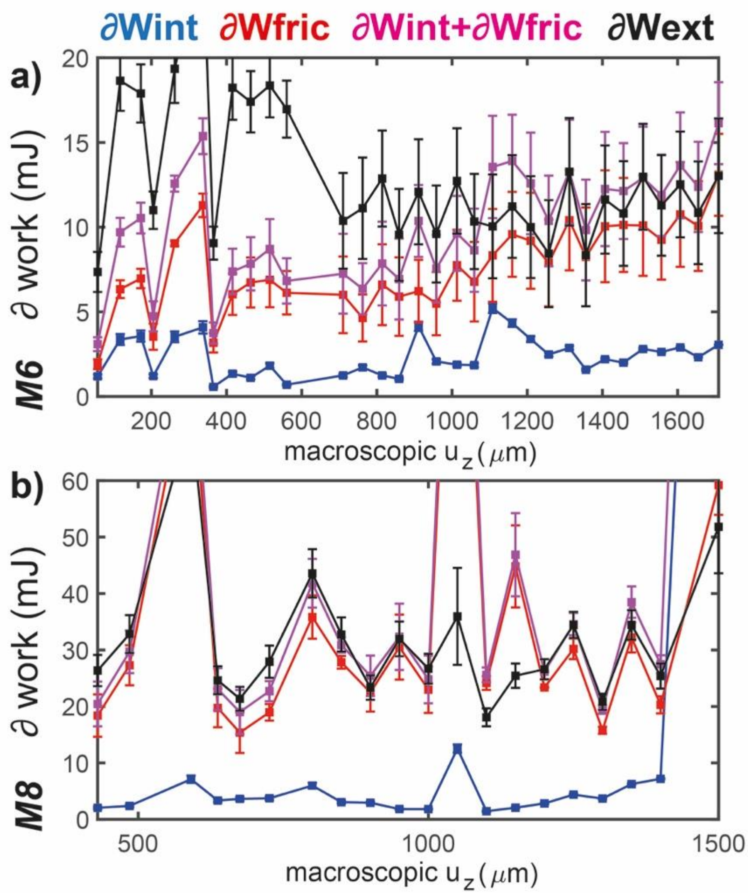

Figure 9

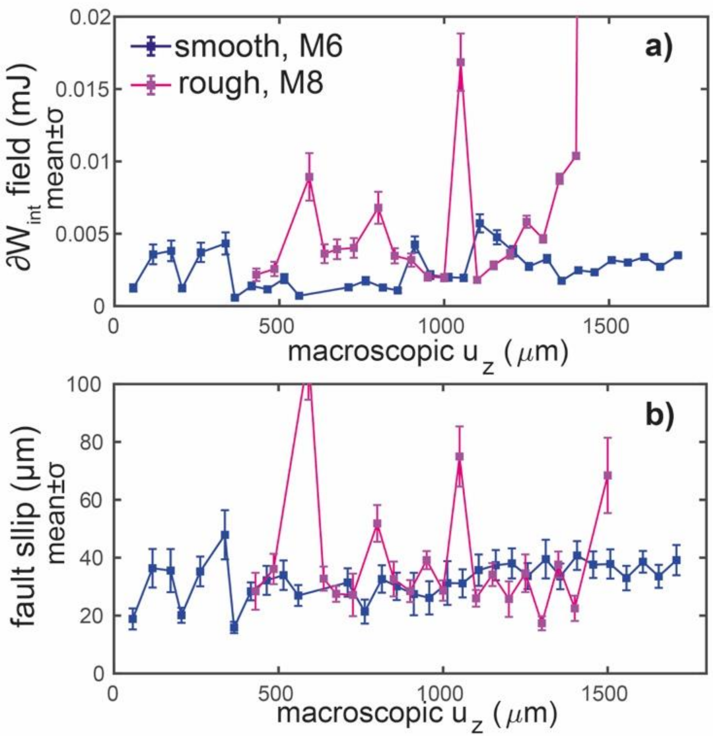

Quantities used to calculate total ∂W_{int} (a) and ∂W_{fric} (b) that exclude the impact of system volume and applied principal stresses. a) ∂W_{int} done in 0.1^2 mm^2 squares throughout system. The sum of the ∂W_{int} done in each of these areas produces the total ∂W_{int}. b) Average fault slip. Vertical bars show range in ∂W_{int} and fault slip measurements. See Methods for details.